Geophysical Research Letters

RESEARCH LETTER
10.1029/2021GL097243

Observation-Based Estimates of Eulerian-Mean Boundary Downwelling in the Western Subpolar North Atlantic

Yingjie Liu[1], Damien G. Desbruyères[1], Herlé Mercier[1], and Michael A. Spall[2]

[1]University of Brest, CNRS, Ifremer, IRD, Laboratoire d'Océanographie Physique et Spatiale, IUEM, Ifremer centre de Brest, Plouzané, France, [2]Woods Hole Oceanographic Institution, Woods Hole, MA, USA

Key Points:

- The long-term mean full-depth density field of the subpolar North Atlantic's boundary is reconstructed from hydrography data
- The along-boundary densification results in a 2.12 ± 0.43 Sv Eulerian-mean downwelling between Denmark Strait and Flemish Cap
- A first observation-based regional and seasonal distribution of near-boundary Eulerian-mean downwelling is provided

Supporting Information:

Supporting Information may be found in the online version of this article.

Correspondence to:

Y. Liu,
yingjie.liu@ifremer.fr

Citation:

Liu, Y., Desbruyères, D. G., Mercier, H., & Spall, M. A. (2022). Observation-based estimates of Eulerian-mean boundary downwelling in the western subpolar North Atlantic. *Geophysical Research Letters*, *49*, e2021GL097243. https://doi.org/10.1029/2021GL097243

Received 3 DEC 2021
Accepted 4 APR 2022

Abstract A significant fraction of the Eulerian-mean downwelling feeding the lower limb of the Atlantic Meridional Overturning Circulation (AMOC) occurs along the subpolar North Atlantic continental slopes and is maintained by along-boundary densification and large-scale geostrophic balance. We here use Argo and shipboard hydrography data to map the 2002–2015 long-term mean density field along the boundary via a dedicated optimal interpolation tool. The overall downstream densification implies an Eulerian-mean downwelling of 2.12 ± 0.43 Sv at 1100 m depth between Denmark Strait and Flemish Cap. A clear regional pattern emerges with downwelling in the Irminger Sea and western Labrador Sea and upwelling along Greenland western continental slope. Comparisons with independent cross-basin estimates confirm that vertical overturning transport across the marginal seas of the subpolar North Atlantic mainly occurs along the continental slopes, and suggest the usefulness of hydrographic data in providing quantitative information about the sinking branch of the AMOC.

Plain Language Summary The Atlantic Meridional Overturning Circulation (AMOC), a critical component of the Earth's climate system due to its role in redistributing heat and freshwater between low and high latitudes, is anticipated to decline over the next century. The downwelling of surface waters in the subpolar North Atlantic that feeds the lower limb of AMOC is a vital yet vulnerable process. As revealed by previous theoretical and modeling work, the overall downstream densification along the boundary results in a significant boundary downwelling. Here, the density along the western boundary between Denmark Strait and Flemish Cap is reconstructed to provide a first observation-based description of the regional and seasonal distribution of this boundary-focused downwelling in the subpolar North Atlantic. This study not only provides valuable insights into how to improve existing ocean circulation theories of overturning but also contributes to a solid benchmark for evaluating how climate models simulate the sinking branch of the AMOC.

1. Introduction

Through its role in redistributing heat, freshwater, and chemical properties between low and high latitudes, the Atlantic Meridional Overturning Circulation (AMOC) is a critical component of Earth's climate system. Warm and saline waters flow from low latitudes toward the poles within the AMOC upper limb. Following significant mixing-driven and surface-forced water mass transformation, colder and fresher waters are returned southward as intermediate and deep-water masses within the AMOC lower limb. Climate model studies indicate that the AMOC could weaken significantly over the next century (IPCC, 2021), and significant efforts have been consequently made over the last decades to understand the processes maintaining the AMOC and the drivers of its variability (e.g., Buckley & Marshall, 2016; Johnson et al., 2019; Lozier, 2012).

The vertical connection between the upper and lower limb of the AMOC, as well as the underlying mechanism, are still under investigation (e.g., Brüggemann & Katsman, 2019; Pedlosky, 2003; Spall & Pickart, 2001; Spall, 2010; Straneo, 2006). The location of this downwelling has long been associated with regions of intense open-ocean convection, such as the Labrador and Irminger seas, where dense and deep waters form because of convective mixing. However, deep convection regions have large vertical heat and salt transports (in density space) but a negligible vertical mass transport (in depth space) (Marshall & Schott, 1999; Send & Marshall, 1995; Spall, 2003, 2004). Instead, the Eulerian-mean downwelling connecting the AMOC upper and lower limbs should occur near continental boundaries, where geostrophy breaks down and a new balance between vertical stretching of planetary vorticity and dissipation of relative vorticity in a thin boundary layer emerges (Spall, 2010). Previous research has established that such downwelling through modification of the boundary current properties

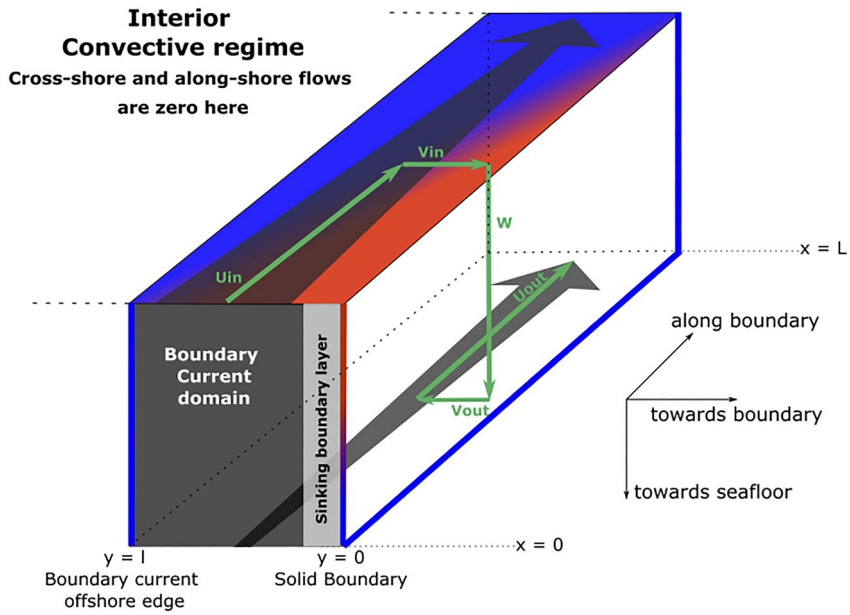

Figure 1. The cooling spiral and associated boundary downwelling. Gray arrows represent the background boundary current. The blue-red shading depicts the horizontal density fields, with the distribution of light waters in red and dense waters in blue giving rise to a cross-shore baroclinic flow in thermal wind balance (V_{in}) fed by the boundary current (U_{in}). Local mass conservation leads to a downward flow at the wall (W), a deep entrainment in the boundary current (V_{out}), and a rapid along-boundary export (U_{out}). The overall effect is a net downwelling within and a barotropization of the boundary current.

in a region is undergoing buoyancy loss (e.g., Cenedese, 2012; Katsman et al., 2018; Spall & Pickart, 2001; Spall, 2010; Straneo, 2006). Notably, the dynamics of Eulerian-mean downwelling are primarily governed by the large-scale geostrophic flow, so that the details of the thin boundary layer where vorticity is ultimately dissipated do not need to be resolved for capturing the overall impact of downwelling (Spall, 2008).

Several studies have focused on the location and underlying mechanism of boundary downwelling. Spall and Pickart (2001) investigated the boundary sinking using a thermodynamic balance. During winter, the boundary current loses heat and buoyancy. As shown schematically in Figure 1, the resulting along-boundary density increase requires a vertically sheared cross-shore baroclinic flow in thermal wind balance (V_{in}) fed by the boundary current itself (U_{in}; there is no exchange with the basin interior). Therefore, the flow rotates counterclockwise with depth along the boundary within a so-called "cooling spiral" To maintain local mass conservation, a net downwelling (W) is required to balance the mass flux toward the boundary. This causes a barotropization of the boundary current, with the upper part decelerating and the lower part accelerating (Spall, 2004, 2008; Straneo, 2006). Without any mean mass flux between the boundary region and the basin interior, the sinking water joins the lower part of the boundary current (V_{out}) and is rapidly exported within the lower limb of AMOC (U_{out}). Thus, the along-boundary pressure (or density) gradient and associated cross-shore geostrophic flow are vital for sinking to occur.

Several processes, including surface buoyancy flux or mean and eddy-driven heat advection, likely contribute to maintaining an along-boundary density gradient. While the respective contribution of these processes is regionally unknown, lateral eddy-driven heat exchanges—generated by the lateral density gradients and baroclinic instability—are widely acknowledged as important in densifying the boundary region, as seen for instance in the Labrador Sea (Katsman et al., 2004; Lilly et al., 2003). Lateral eddy-induced heat fluxes are required to balance the heat loss to the atmosphere and restratify open-ocean water columns following deep convection events (Chanut et al., 2008; Hátún et al., 2007; Katsman et al., 2004; Kawasaki & Hasumi, 2014; Tagklis et al., 2020). Additionally, eddies contribute to interior downwelling and boundary current barotropization through along-isopycnal water masses stirring and exchange between the boundary current and the interior (Brüggemann & Katsman, 2019; Khatiwala & Visbeck, 2000).

Recent studies have used realistic and high-resolution model simulations to investigate the net downwelling in the entire Subpolar Gyre (SPG) (Katsman et al., 2018; Sayol et al., 2019) or in marginal seas characterized by high convective activity, such as the Labrador Sea (Brüggemann & Katsman, 2019; Georgiou et al., 2019). Katsman et al. (2018) and Sayol et al. (2019) confirmed that the bulk of the vertical volume flux occurs along the boundary and that its spatial integral in the SPG is close to the magnitude of the AMOC—the zonally integrated meridional flow—at the southern exit of the SPG (i.e., near 45°N). Katsman et al. (2018) further demonstrated that the amount of boundary sinking is largely determined by density change, except in the region where eddy-driven processes or hydraulic controls may become significant. The role of eddy-driven processes was particularly studied by Brüggemann and Katsman (2019) and Georgiou et al. (2019), who showed the importance of eddies in balancing heat loss over the Labrador Sea and in triggering boundary downwelling along steepened isopycnal surfaces.

Estimates of boundary-focused sinking and its associated mechanisms from in situ observations are still lacking. Here, we use hydrography data from global ocean monitoring programs (e.g., Argo, go-ship) to estimate for the first time the long-term Eulerian-mean along-boundary downwelling and its spatial and seasonal distribution within the western SPG, from Denmark Strait (DKS) to Flemish Cap (FC). While such observations cannot resolve the intricate and small-scale dynamics of downwelling within the thin boundary layer where it is most likely to occur, they can be used to infer the large-scale geostrophic balance governing it.

We begin by introducing a specific optimal interpolation method to map temperature and salinity along the boundary, and then describe the method used for calculating cross-shore velocities and resulting vertical transport (Section 2). Section 3 describes the reconstruction of the along-boundary density field, as well as the subsequent calculation of geostrophic velocity and associated downwelling. A summary and a discussion conclude this study (Section 4).

2. Data and Methodology

2.1. Data

We use three datasets of temperature and salinity profiles to map the long-term mean (2002–2015) and seasonal cycle of hydrographic properties in the SPG (52–66°N; 30°W–66°W): the In Situ Analysis System-ISAS15 (Gaillard et al., 2016; Kolodziejczyk et al., 2021), the Coriolis data set for ReAnalysis-CORA (Cabanes et al., 2013; Szekely et al., 2019), and EN4.4.2.2 (Good et al., 2013). Whereas ISAS15 only contains Argo profiles, EN4 and CORA include profiles from fixed moorings and shipboard full-depth CTD profiles. These profiles have undergone quality control checks in delayed mode, and we only use *good* profiles (i.e., fully acceptable). Because most Argo floats drift at 1000 m depth, ISAS15 exhibits an uneven distribution across the domain with decreasing near the shelf (see Figure S1 in Supporting Information S1). The EN4 and CORA provide adequate coverage of profiles near the shelf. The temperature and salinity fields are then used to derive the in situ (ρ) and potential (σ_0) density fields. Bathymetry is derived from ETOPO2.

2.2. Optimal Interpolation

Optimal interpolation (OI) is a frequently used technique for generating gridded property fields from sparse and irregular data (Bretherton et al., 1976; Kaplan et al., 1997). The conventional OI algorithms for climatological mapping use circle-shaped Gaussian correlation functions (see Gaillard et al., 2016 for additional details), but we herein employ an elliptic Gaussian correlation function parallel to isobaths, with length scales of 67 km (cross-shore axis) and 145 km (along-shore axis) to account for the larger (smaller) correlation length scales in the along-shore (cross-shore) directions. In other words, this provides data along the boundary current's primary path with larger weights in the estimation. Based on convergence sensitivity tests, the horizontal resolution is set as 4 km, which enables us to refine the properties along boundaries and topographic features (such as the sharpest portions of the continental slope). Interpolation is conducted at 152 levels independently between 0 and 2000 m; the vertical spacing is 5 m down to 100 m, 10 m down to 800 m, and 20 m below. The configuration of the OI is explained in more detail in Gaillard et al. (2016). The overall mapping methodology was eventually validated by good performance in estimating properties along the OVIDE and AR7W hydrographic lines (see Figure S2–S5 in Supporting Information S1). To estimate the vertical transport, the final multiproduct mappings of temperature and salinity for the four seasons (Winter (January–March), Spring (April–June), Summer (July–September),

Autumn (October–December)) is the average of the fields derived independently from the three datasets. The density below 2000 m is obtained by linear extrapolation from the above 2000 m. The three-dimensional density field is eventually interpolated onto the locations of 100 m-spaced isobaths spanning 700 to 3000 m from DKS to FC.

2.3. Computing Cross-Shore Geostrophic Velocity and the Vertical Transport

To calculate the absolute geostrophic cross-shore velocity, a local mass balance assumes equal inshore and offshore transport. Any horizontal recirculations between the boundary current and the interior are assumed to be mostly barotropic, with no effect on the cross-shore baroclinic density field. These assumptions are supported by laboratory experiments showing that water downwelling along a vertical wall returns offshore in the opposite direction (Cenedese, 2012), and by observations of the strong barotropic nature of inner gyres and lateral entrainments (Våge et al., 2011). The baroclinic component of the cross-shore velocity relative to the sea surface ($v_{baroclinic}$) is first derived from the along-boundary density gradient and the thermal wind balance:

$$\frac{\partial v_{baroclinic}(x,y,z)}{\partial z} = -\frac{g}{\rho_0 f}\frac{\partial \rho(x,y,z)}{\partial x} \tag{1}$$

where x, y, and z represent the along-shore, cross-shore, and vertical directions, respectively. g is 9.8 m/s^2, ρ is the *in-situ* density field derived from OI, ρ_0 is 1024 kg/m^3, and f is 1.26×10^{-4} s^{-1}.

The reference velocity $v_{reference}$ is then obtained by applying the local *zero-mass transport constraint*:

$$v_{reference}(x,y) = \frac{-\int_{H(x,y)}^{0} (v_{baroclinic}(x,y,z))\,dz}{\Delta z} \tag{2}$$

where H (x,y) denotes the bottom depth and Δz the water depth.

We calculate vertical transport along the SPG at isobaths ranging from 700 to 3,000 m with a 100 m interval. The analysis focuses offshore of the 700 m isobath because of poorer sampling inshore. This has little effect on the maximum transport estimate, however, which is found across much deeper slope. For a given isobath (y_0), the vertical transport stream function $\psi(z)$ is estimated as follows:

$$\psi(y_0, z) = \int_{x_u}^{x_d}\int_{z}^{0} \left(v_{baroclinic}\left(x, y_0, z'\right) + v_{reference}\left(x, y_0\right)\right) dz'dx \tag{3}$$

where x_u and x_d are the upstream and downstream locations along a given isobath y_0. The maximum of ψ (y_0, z) represents the net shoreward transport integrated along an isobath between x_u and x_d. The maximum vertical transport is thus defined as the maximum of the net shoreward transport ψ_{max} across the 100-m spaced isobaths between 700 and 3,000 m.

A Monte Carlo approach is used to add an uncertainty estimate to our mean vertical transport calculation. We use the errors estimated from the OI calculation, which depend on the distribution density and variability of adjacent profiles, to perturb the temperature and salinity fields randomly and re-compute overturning stream functions. 12,000 bootstrap estimates of the stream functions in four seasons are calculated using 3,000 iterations on the three datasets. The errors of the transport are considered as two times the standard deviation of the 12,000 estimates (see Figure S6 in Supporting Information S1).

3. Results

Figure 2 shows the multiproduct long-term mean temperature field averaged over the upper 300 m depth. It depicts the cooling of the warm boundary current in the upper layer as it flows from DKS to FC. The full-depth surface-referenced in situ (ρ) and potential (σ_0) fields are determined along 100 m-spaced isobaths ranging from 700 to 3000 m. The 2400 m isobath is shown here (for the reason that will become obvious later) and labeled using the distance relative to the isobath's total length (4,032 km), starting at s = 0 near the DKS at −30°W and ending at s = 1 near FC at −48°W.

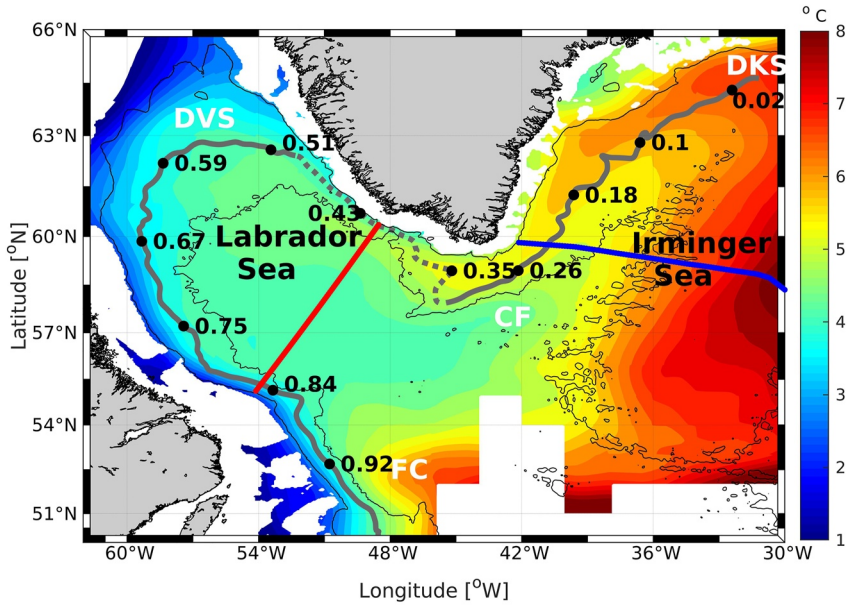

Figure 2. Observed multiproduct time-mean (2002–2015) temperature field averaged in upper 300 m as obtained from an optimal interpolation tool specifically designed for the boundary region (see Section 2.2). The isobaths 700 and 3,000 m are shown as thin black contours, and the isobath 2400 m (thick black line) is used in Figure 3 to show along-boundary density and velocity fields, from s = 0 at Denmark Strait (DKS) until s = 1 at Flemish Cap. Solid and dashed portions of this contour refer to (Eulerian) downwelling and upwelling regions. Key locations noted in the plot are DKS, Cape Farewell (CF), Davis Strait (DVS), and Flemish Cape (FC). Red line indicates the AR7W section, whereas the blue line indicates the OVIDE section.

Figures 3a and 3b depicts the density and associated cross-shore geostrophic velocity sections following isobath 2400 m from DKS to FC (the along-isobath baroclinic and reference velocities in Equation 2 are shown in Figure S8 in Supporting Information S1). The density generally increases downstream (Figures 3a and 3c) and is primarily determined by the change in along-shore temperature (see Figure S7 in Supporting Information S1). The density of the upper (above 300 m) and intermediate layer (300–1500 m) gradually increases from s = 0 to s = 0.3, while it decreases from s = 0.3 until the east of Davis Strait (DVS) (s = 0.5) (Figure 3c). Downstream of DVS, the density in the intermediate layer increases again but remains constant in the upper layer. Overall, even though the density in the upper layer remains constant, the increase in density in the intermediate layer along isobath 2400 m from 27.71 kg m^{-3} to 27.74 kg m^{-3} should expectedly drive an overall downwelling. The resulting cross-shore absolute geostrophic velocity (Figure 3b) shows the water flows inshore (offshore) and offshore (inshore) in the upper and lower layers, driving downwelling (upwelling). There are two levels of no motion at some boundary locations due to more complex changes of stratification (induced by the freshwater inflow near DVS, for instance). The level of no motion is deeper in the Irminger Sea than in the Labrador Sea and ranges from 500 to 1500 m depth.

A vertical section of the DKS-FC along-shore average of the cross-shore velocity crossing different isobaths is shown in Figure 4a. It reveals a cell-like structure in the upper and lower layers, with a cell center in the isobath 2400 m at 100 m depth. In line with theory and experimental works (Cenedese, 2012; Spall, 2008), the cross-shore velocity increases from the coast offshore to a maximum near the 2400 m isobath and then decreases offshore until the along-shore density gradient becomes insignificant at circa the 3,000 m isobath. The mean maximum vertical transport along the SPG boundary is 2.12 Sv at 1088 m, with an uncertainty of 0.43 Sv (2 times STD) estimated from 12,000 bootstrap estimates. The transport in density space is 2.11 ± 0.28 Sv by crossing the nearly horizontal 27.73 kg m^{-3} isopycnal surface. Note that this does not fully account for water mass formation near the boundary since the diapycnal flux is also carried out by the along-stream densification in the upper layer and cross-stream eddy circulation in the deeper layer (Brüggemann & Katsman, 2019).

The cumulative transport (Figure 3c) along the 2400 m isobath reveals that the entire DKS-FC boundary can be divided into three distinct areas: a downwelling region in the Irminger Sea (ID, s = 0 to s = 0.33), an upwelling

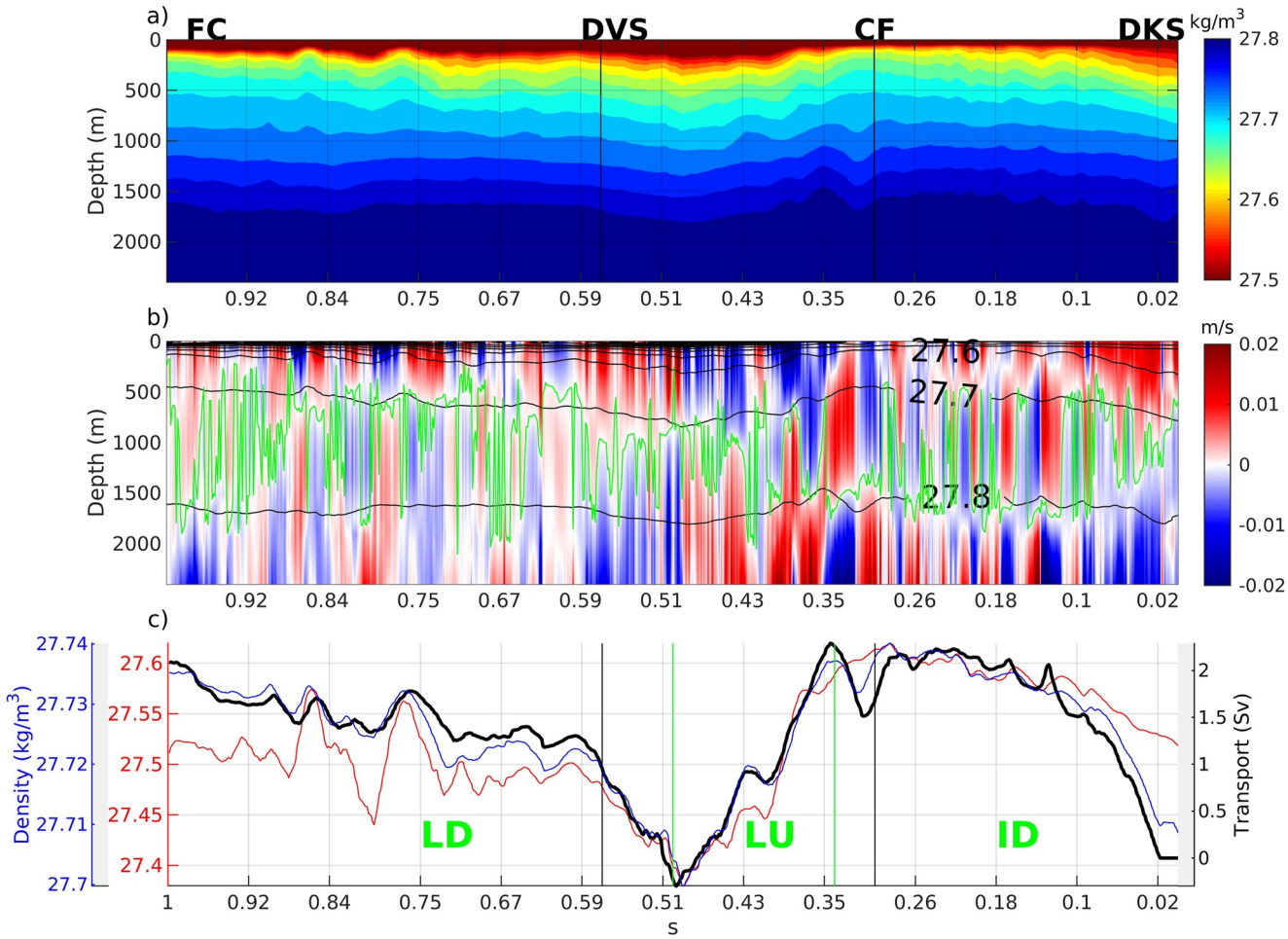

Figure 3. (a) Optimal interpolation-derived multiproduct density (σ_0) field along isobath 2400 m. (b) The cross-shore geostrophic velocity field along isobath 2400 m. The positive (negative) values indicate inshore (offshore) flows. The green line indicates the depth at which the maximum (accumulated) vertical transport is found (i.e., levels of no motion). The σ_o = 27.6, 27.7, 27.8 kg m^{-3} isopycnals are contoured in black. (c) The density along the boundary from s = 0 to s = 1 averaged in the upper layer (1–300 m, red curve) and the intermediate layer (301–1500 m, blue curve). The maximum vertical transport (black curve) accumulated along the boundary from s = 0 to s = 1. The upward slopes indicate the downwelling (LD-Labrador Downwelling, s = 0.5–1, ID-Irminger Downwelling, s = 0–0.33), and the downward slope indicates upwelling (LU-Labrador Upwelling, s = 0.33–0.5).

region in the eastern Labrador Sea (LU, s = 0.33 to s = 0.5), and a downwelling region in the western Labrador Sea (LD, s = 0.5 to s = 1). These downwelling/upwelling patterns result from the downstream density increase/decrease along the boundary (Figure 3c). The cross-shore velocities averaged along the isobaths in these three regions are shown in Figures 4d, 4g and 4j. They also capture cell-like structures within the boundary current system, with waters flowing inshore (offshore) in the upper layer and offshore (inshore) in the lower layer of the downwelling (upwelling) region. Maximum cross-shore transports, which are consistently observed at the 2400 m isobath, are of comparable magnitude in each of the three regions, with upwelling (2.17 Sv) along the western slope of Greenland balancing half of the total downwelling (4.28 Sv) (Figure 4e, 4h and 4k).

Water sinks (upwells) all year in the downwelling (upwelling) regions. The Eulerian-mean transport in the LD region is 2.23 ± 0.71 Sv (Figures 4e and Table 1) at a depth of 986 m. The transport in the LU region (Figures 4h and Table 1) is 2.17 ± 0.74 Sv at a depth of 1182 m. The ID has similar downwelling of 2.05 ± 0.79 Sv to the LD (Figures 4k and Table 1) at a depth of 1304 m. The regional density-space transport follows a very similar pattern to that in depth-space, and the density level of maximum transport remains nearly constant at around 27.71–27.76 kg/m^{-3}. The uncertainty estimates in Table 1 show the standard deviations calculated from 3,000 iterations using the three datasets. Seasonal and regional errors are all between 0.3 and 0.8 Sv. The seasonal variations are of the same magnitude as the uncertainties derived from the bootstrap estimates based on the three datasets, and

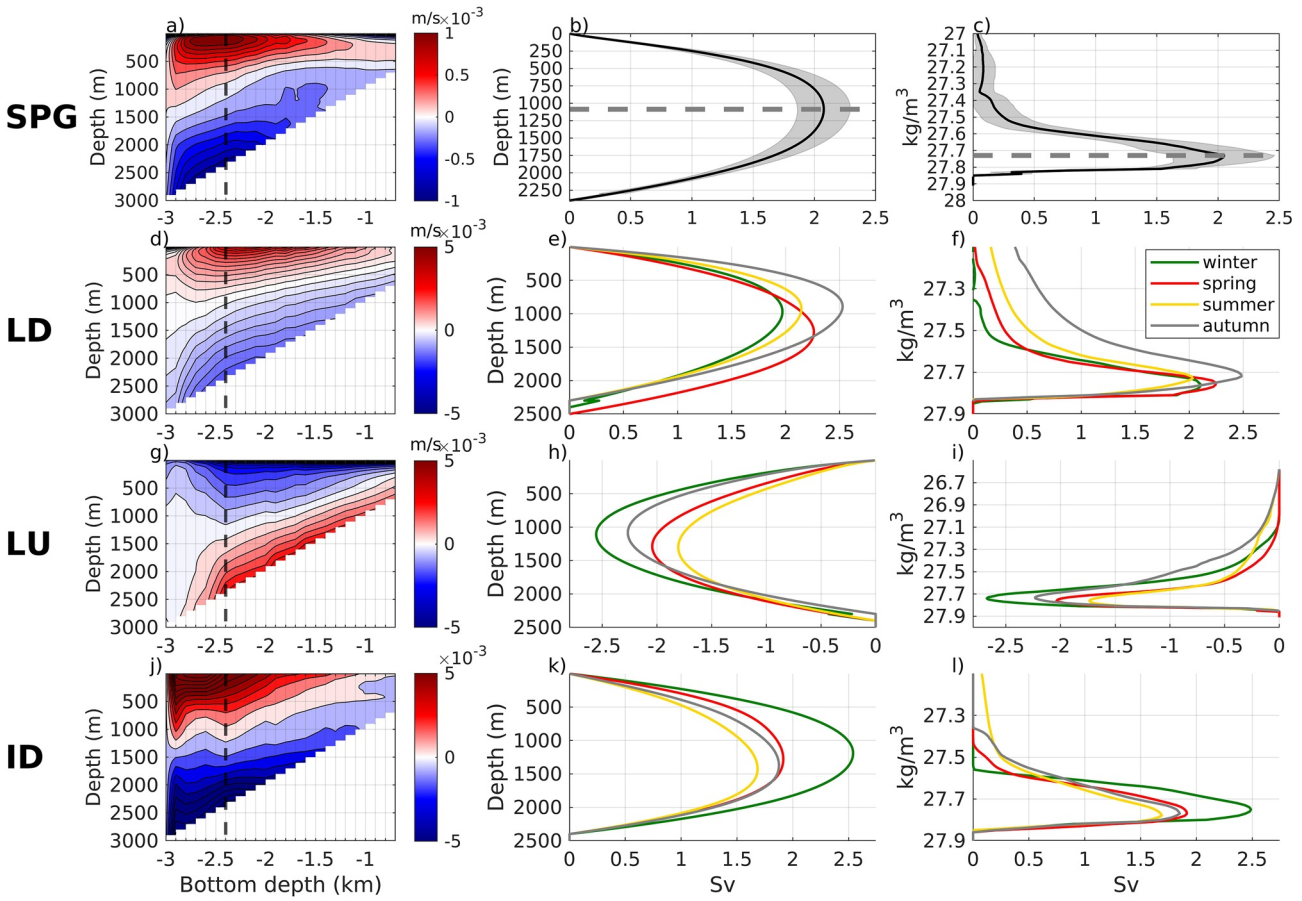

Figure 4. (a) The along-shore average of the cross-shore velocity along the Subpolar Gyre averaged at the 100 m-spaced isobaths between 700 and 3,000 m. The x-axis represents distinct isobaths rather than the cross-shore distance. The dashed line indicates the isobath (2400 m) where the maximum vertical transport is found. (b and c) The corresponding geostrophic stream functions obtained by accumulating the vertical transport from the surface in depth space and density space. The errors in gray patch are one standard deviation derived from the bootstrap simulations. The dashed lines indicate the depth (density) of maximum overturning. Panels (d–l) are the same as (a–c), but for the three regions defined in Figures 1 and 2c and for the four seasons: Winter (January–March), Spring (April–June), Summer (July–September), Autumn (October–December). The uncertainty estimates and maximum overturning depths for each region are represented in Table 1.

the present estimates of seasonal changes of the Eulerian-mean downwelling are not statistically significant for the whole SPG or individual basins. This is in line with Li et al. (2021), who did not detect a statistically significant signal cycle when estimating the composite monthly mean MOC transport using the OSNAP program's 46-month records. Furthermore, Sayol et al. (2019) used a high-resolution model to find that seasonal variability

Table 1
The Maximum Vertical Transport (Sv) Derived From the Multiproduct Mean in the Labrador Downwelling (LD), Labrador Upwelling (LU) and Irminger Downwelling (ID) Regions (Defined in Figure 2) and Whole Subpolar Gyre (SPG)

Season	LD	LU	ID	SPG
Winter	1.97 ± 0.30 (970)	−2.56 ± 0.44 (1108)	2.57 ± 0.31 (1190)	**1.99 ± 0.58** (975)
Spring	2.27 ± 0.31 (1274)	−2.04 ± 0.31 (1288)	1.92 ± 0.61 (1278)	**2.14 ± 0.81** (1253)
Summer	2.16 ± 0.28 (923)	−1.81 ± 0.34 (1301)	1.84 ± 0.84 (1425)	**2.19 ± 0.82** (903)
Autumn	2.54 ± 0.51 (891)	−2.27 ± 0.60 (1084)	1.88 ± 0.45 (1372)	**2.14 ± 0.47** (1044)
Annual	**2.23 ± 0.71 (986)**	**−2.17 ± 0.74** (1182)	**2.05 ± 0.79** (1304)	**2.12 ± 0.43** (1088)

Note. The errors are two times of standard deviation derived from the bootstrap simulations. The depths (m) of the maximum transport are displayed in parentheses.

in boundary sinking is rather insignificant in comparison to interior sinking, and that the variability is thought to be driven by ageostrophic dynamics that our large-scale geostrophic balance cannot capture. Nevertheless, based on our observations, a potential upper bound on the seasonal cycle amplitude has been established.

4. Discussion and Conclusion

We have provided here a first observation-based estimate of the Eulerian-mean downwelling along the boundary of the SPG. Using in situ temperature and salinity profiles from sustained global ocean observational networks, we mapped the long-term mean density along the continental slope from the Denmark Strait to Flemish Cap. The cooling and resulting densification along the boundary region result in a geostrophic cross-shore flow and a downwelling above the continental slope, with a maximum value of 2.12 ± 0.43 Sv at 1,100 m depth. The transport in density space, which is here representative of the cross-shore diapycnal flux, is very similar to the transport in depth space. Cross-shore velocity is found to increase offshore and peak near the 2,400 m isobath, before eventually disappearing near the 3,000 m isobath, in good agreement with observation-based descriptions of the distinct circulation of the interior and the boundary current (Pacini et al., 2020), and with theoretical or modeling works suggesting limited mean advective exchanges between those two regimes (Brüggemann & Katsman, 2019; Cenedese, 2012). Our analysis further reveals no strong or statistically significant seasonality in the magnitude of downwelling across the entire SPG.

Interestingly, the total Eulerian-mean downwelling from CF to FC is estimated as only 0.1 ± 0.03 Sv due to compensation between upwelling along the western slope of Greenland and downwelling in the remaining portion of the Labrador Sea. Downwelling was estimated to be 1.4 Sv in that region by Katsman et al. (2018) in high-resolution simulations. Western Greenland is in fact generally described as a region with strong along-shore densification due notably to eddy-driven heat flux, as described in several modeling works (Georgiou et al., 2019; Katsman et al., 2004). This apparent discrepancy could arise for several reasons. Warming in the intermediate layer might be overly represented due to an uneven distribution of profiles along western Greenland's narrowing boundary, which may be insufficient to represent the boundary current's features. It is also possible that the subsurface warming along western Greenland (also observed in other estimates, see, e.g., Palter et al., 2008) indicates a signal of restratification following baroclinic instability. The tilted isopycnals on the offshore side of an unstable current should deepen downstream and drive a warming signal in this portion of the water column. Additionally, the cross-shore transport along the narrowing boundary might represent the deflection of upper layer water into the interior. An offshore mass flux, resulting from either a flux of less dense water off the shelf or a broadening of the boundary current due to baroclinic instability, would be diagnosed as upwelling because of the assumption of no net flow across the isobaths. Future work may focus on describing the properties in shallower depths further inshore when sampling is denser. Nevertheless, the net downwelling in SPG is not sensitive to the distribution of boundary downwelling or upwelling, as demonstrated by the fact that the strong downstream warming and subsequent upwelling in the eastern Labrador Sea are compensated by the significant downstream cooling and subsequent downwelling in the western Labrador Sea. Indeed, the full-basin integrated downwelling only depends on the density variation between the DKS and FC and thus remains a robust estimate.

Further comparison with independent overturning estimates from cross-basin arrays or realistic modeling provides insights and confidence in the values reported herein. The Irminger Sea downwelling is estimated to be 2.05 ± 0.79 Sv at 1200 m depth, in line with the high-resolution modeling estimates of 1.4 Sv from Katsman et al. (2018) and 1.13 Sv from Sayol et al. (2019) within uncertainty estimates. Summer downwelling in the Labrador Sea is estimated to be 0.85 ± 0.15 Sv at depth 685 m by integrating the transport between the two ends of the AR7W line (Figure 2), which agrees quantitatively with Pickart and Spall (2007) observation-based meridional transports of about 1 Sv at depth 800 m. The annual mean downwelling rate in the Labrador Sea is estimated here as 0.72 ± 0.07 Sv, similar to Holte and Straneo's (2017) and Lozier et al. (2019) observations, which amount to 0.9 and 0.8 Sv, respectively. This also confirms that the majority of sinking occurs near the Labrador Sea's boundary, with little vertical mass transport occurring in the convective interior.

Furthermore, we quantify here only the western boundary downwelling downstream of DKS, omitting potential upstream contributions around Reykjanes Ridge (RR) or the Rockall Plateau, for instance. The zero-mass constraint used herein to estimate cross-shore overturning is likely inadequate in such regions where the vertical integral of the cross-shore geostrophic flow is not zero (consider for instance the net westward flow above the crest of RR). Addi-

tionally, overflows across the DKS or the Iceland-Scotland Ridge contribute significantly to the overall net sinking in the SPG—about 7 Sv (Hansen & Østerhus, 2000)—via hydraulically controlled dynamics not captured by our geostrophic estimate. A refinement of the boundary sinking calculation is being investigated for these specific areas.

Ekman transport was estimated from the long-term mean (2002–2015) along-shore wind stress averaged from the NCEP/NCAR Reanalysis 1 and ERA5 data set. It carries 0.7–0.9 Sv of water inshore of the DKS-FC boundary. Two-dimensional models require that this onshore flow returns to the basin interior (e.g., Choboter et al., 2011; Lentz & Chapman, 2004), but three-dimensional models with spatially variable winds (or coastlines) demonstrate that some of this water flows along the shelf (e.g., Allen, 1976; Suginohara, 1982). It is difficult to determine a priori the partition of this downwelled water between along-shelf and interior pathways as it will depend on various factors such as stratification, topography, nonlinearity, wind pattern, etc. However, any of the Ekman transport that does flow back into the interior will remain relatively shallow and have a negligible effect on the deep overturning circulation, and so is not included in our estimate.

We finally emphasize that novel descriptions of the Eulerian-mean downwelling rooted in observations are critical for understanding AMOC variability in the current context of anthropogenic climate change (IPCC, 2021). Both upper-ocean warming and increased ice melting may significantly affect along-boundary density gradients and result in the reduced sinking and a consequent weakening of the AMOC. A better observation-based understanding of boundary-focused vertical transport may also help us to properly represent or parameterize the details of the underlying boundary dynamics in climate models. It can assist in not only describing the circulation and diagnosing its controls, but also in providing valuable insights into how to improve existing ocean circulation theories of overturning.

Data Availability Statement

The In Situ Analysis System-ISAS15 data set (2002–2015) is available from the SEANOE repository (https://www.seanoe.org/data/00412/52367/, last access: July 2021) and described in Gaillard et al. (2016). The Coriolis data set for ReAnalysis-CORA V5.2 (1950-to present) is available from the SEANOE repository (https://www.seanoe.org/data/00351/46219/, last access: September 2019) and described in Szekely et al. (2019). The EN4.4.2.2 data set for years 1990 to present is provided by Met Office Hadley Centre and available at https://www.metoffice.gov.uk/hadobs/en4/ (last access: November 2021) and described in Good et al. (2013). The A25-Ovide and AR7W hydrography sections are available via the CLIVAR and Carbon Hydrographic Data Office (CCHDO) platform (https://cchdo.ucsd.edu/). The NCEP/NCAR Reanalysis 1 (1948/01/01 to present) is provided in National Centers for Environmental Prediction (/data/gridded/data.ncep.reanalysis.html) and described in Kalnay et al., (1996). The ERA5 data set (1950-to present) is available in Copernicus Climate Change Service Climate Data Store (CDS), https://cds.climate.copernicus.eu/cdsapp#!/home. The present analysis does not use new unpublished data.

Acknowledgments
We greatly appreciate the reviewers for their constructive comments. Yingjie Liu and Damien G. Desbruyères are funded by IFREMER (Institut Français de Recherche pour l'Exploitation de le Mer), Herlé Mercier is funded by CNRS (the French Centre National de la Recherche Scientifique), and Michael A. Spall is funded by NSF (National Science Foundation) Grant OCE-1947290 and NSF Grant OCE-1922538. This work was carried out within the framework of the NAOS and ARGO-2030 projects. The two projects received the support of the French government within the framework of the "Investissements d'avenir" program managed by the Agence Nationale de la Recherche (ANR) under the references ANR-10-EQPX-40 and ANR-21-ESRE-0019. The authors thank all colleagues and ship crews involved in the OVIDE cruises during which the hydrography data were obtained. The OVIDE project was supported by CNRS, Ifremer, the national program LEFE (Les Enveloppes Fluides et l'Environnement) and the Spanish Ministry of Sciences and Innovation co-funded by the Fondo Europeo de Desarrollo Regional 2007–2012 (FEDER) through the CATARINA project (CTM2010-17141).

References

Allen, J. S. (1976). Some aspects of the forced wave response of stratified coastal regions. *Journal of Physical Oceanography*, *6*, 113–119. https://doi.org/10.1175/1520-0485(1976)006<0113:saotfw>2.0.co;2

Bretherton, F. P., Davis, R. E., & Fandry, C. B. (1976). A technique for objective analysis and design of oceanographic experiments applied to MODE-73. *DeepSea Res*, *23*, 559–582. https://doi.org/10.1016/0011-7471(76)90001-2

Brüggemann, N., & Katsman, C. A. (2019). Dynamics of downwelling in an eddying marginal sea: Contrasting the eulerian and the isopycnal perspective. *Journal of Physical Oceanography*, *49*(11), 3017–3035. https://doi.org/10.1175/JPO-D-19-0090.1

Buckley, M. W., & Marshall, J. (2016). Observations, inferences, and mechanisms of Atlantic meridional overturning circulation variability: A review. *Reviews of Geophysics*, *54*, 5–63. https://doi.org/10.1002/2015RG000493

Cabanes, C., Grouazel, A., Von Schuckmann, K., Hamon, M., Turpin, V., & Coatanoan, C. (2013). The CORA dataset: Validation and diagnostics of in-situ ocean temperature and salinity measurements. *Ocean Science*, *9*(1), 1–18. https://doi.org/10.5194/os-9-1-2013

Cenedese, C. (2012). Downwelling in basins subject to buoyancy loss. *Journal of Physical Oceanography*, *42*(11), 1817–1833. https://doi.org/10.1175/JPO-D-11-0114.1

Chanut, J., Barńier, B., Large, W., Debreu, L., Penduff, T., Molines, J. M., & Mathiot, P. (2008). Mesoscale eddies in the Labrador Sea and their contribution to convection and restratification. *Journal of Physical Oceanography*, *38*(8), 1617–1643. https://doi.org/10.1175/2008JPO3485.1

Choboter, P. F., Duke, D., Horton, J. P., & Sinz, P. (2011). Exact solutions of wind-driven coastal upwelling and downwelling over sloping topography. *Journal of Physical Oceanography*, *41*(7), 1277–1296. https://doi.org/10.1175/2011JPO4527.1

Gaillard, F., Reynaud, T., Thierry, V., Kolodziejczyk, N., & Von Schuckmann, K. (2016). In situ-based reanalysis of the global ocean temperature and salinity with ISAS: Variability of the heat content and steric height. *Journal of Climate*, *29*(4), 1305–1323. https://doi.org/10.1175/JCLI-D-15-0028.1

Georgiou, S., van der Boog, C. G., Brüggemann, N., Ypma, S. L., Pietrzak, J. D., & Katsman, C. A. (2019). On the interplay between downwelling, deep convection and mesoscale eddies in the Labrador Sea. *Ocean Modelling*, *135*, 56–70. https://doi.org/10.1016/j.ocemod.2019.02.004

Good, S. A., Martin, M. J., & Rayner, N. A. (2013). EN4: Quality controlled ocean temperature and salinity profiles and monthly objective analyses with uncertainty estimates. *Journal of Geophysical Research: Oceans*. https://doi.org/10.1002/2013JC009067

Hansen, B., & Østerhus, S. (2000). North Atlantic-Nordic Seas exchanges. *Progress in Oceanography*, *45*(2), 109–208. https://doi.org/10.1016/S0079-6611(99)00052-X

Hátún, H., Eriksen, C. C., & Rhines, P. B. (2007). Buoyant eddies entering the Labrador Sea observed with gliders and altimetry. *Journal of Physical Oceanography*, *37*(12), 2838–2854. https://doi.org/10.1175/2007JPO3567.1

Holte, J., & Straneo, F. (2017). Seasonal overturning of the Labrador Sea as observed by Argo floats. *Journal of Physical Oceanography*, *47*(10), 2531–2543. https://doi.org/10.1175/JPO-D-17-0051.1

IPCC. (2021). In V. P. Zhai, A. Pirani, S. L. Connors, C. Péan, S. Berger, N. Caud, et al. (Eds.), *Climate change 2021: The physical science basis. Contribution of working group I to the sixth assessment report of the intergovernmental panel on climate change [Masson-Delmotte]*. Cambridge University Press.

Johnson, H. L., Cessi, P., Marshall, D. P., Schloesser, F., & Spall, M. A. (2019). Recent contributions of theory to our understanding of the Atlantic meridional overturning circulation. *Journal of Geophysical Research: Oceans*, *124*(8), 5376–5399. https://doi.org/10.1029/2019JC015330

Kalnay, E., Kanamitsu, M., Kistler, R., Collins, W., Deaven, D., Gandin, L., et al. (1996). The NCEP/NCAR 40-year reanalysis project. *Bulletin of the American Meteorological Society*, *77*(3), 437–471. https://doi.org/10.1175/1520-0477(1996)077<0437:tnyrp>2.0.co;2

Kaplan, A., Kushnir, Y., Cane, M., & Blumenthal, B. (1997). Reduced space optimal analysis for historical data sets: 136 years of Atlantic sea surface temperature. *Journal of Geophysical Research*, *102*, 27853–27860. https://doi.org/10.1029/97jc01734

Katsman, C. A., Drijfhout, S. S., Dijkstra, H. A., & Spall, M. A. (2018). Sinking of dense North Atlantic waters in a global ocean model: Location and controls. *Journal of Geophysical Research: Oceans*, *123*(5), 3563–3576. https://doi.org/10.1029/2017JC013329

Katsman, C. A., Spall, M. A., & Pickart, R. S. (2004). Boundary current eddies and their role in the restratification of the Labrador Sea. *Journal of Physical Oceanography*, *34*(9), 1967–1983. https://doi.org/10.1175/1520-0485(2004)034<1967:bceatr>2.0.co;2

Kawasaki, T., & Hasumi, H. (2014). Effect of freshwater from the West Greenland current on the winter deep convection in the Labrador Sea. *Ocean Modelling*, *75*, 51–64. https://doi.org/10.1016/j.ocemod.2014.01.003

Khatiwala, S., & Visbeck, M. (2000). An estimate of the eddy-induced circulation in the Labrador Sea. *Geophysical Research Letters*, *27*(15), 2277–2280. https://doi.org/10.1029/1999GL011073

Kolodziejczyk, N., Prigent-Mazella, A., & Gaillard, F. (2021). ISAS temperature and salinity gridded fields. *SEANOE*. https://doi.org/10.17882/52367

Lentz, S. J., & Chapman, D. C. (2004). The importance of nonlinear cross-shelf momentum flux during wind-driven coastal upwelling. *Journal of Physical Oceanography*, *34*(11), 2444–2457. https://doi.org/10.1175/jpo2644.1

Li, F., Lozier, M. S., Bacon, S., Bower, A. S., Cunningham, S. A., de Jong, M. F., et al. (2021). Subpolar North Atlantic western boundary density anomalies and the meridional overturning circulation. *Nature Communications*, *12*(1). https://doi.org/10.1038/s41467-021-23350-2

Lilly, J. M., Rhines, P. B., Schott, F., Lavender, K., Lazier, J., Send, U., & D'Asaro, E. (2003). Observations of the Labrador Sea eddy field. *Progress in Oceanography*, *59*(1), 75–176. https://doi.org/10.1016/j.pocean.2003.08.013

Lozier, M. S. (2012). Overturning in the North Atlantic. *Annual Review of Marine Science*, *4*, 291–315. https://doi.org/10.1146/annurev-marine-120710-100740

Lozier, M. S., Li, F., Bacon, S., Bahr, F., Bower, A. S., Cunningham, S. A., et al. (2019). A sea change in our view of overturning in the subpolar North Atlantic. *Science*, *363*, 516–521. https://doi.org/10.1126/science.aau6592

Marshall, J., & Schott, F. (1999). Open-ocean convection: Observations, theory, and models. *Reviews of Geophysics*, *37*(1), 1–64. https://doi.org/10.1029/98RG02739

Pacini, A., Pickart, R. S., Bahr, F., Torres, D. J., Ramsey, A. L., Holte, J., et al. (2020). Mean conditions and seasonality of the West Greenland boundary current system near cape farewell. *Journal of Physical Oceanography*, *50*(10), 2849–2871. https://doi.org/10.1175/JPO-D-20-0086.1

Palter, J. B., Lozier, M. S., & Lavender, K. L. (2008). How does Labrador Sea water enter the deep western boundary current? *Journal of Physical Oceanography*, *38*(5), 968–983. https://doi.org/10.1175/2007JPO3807.1

Pedlosky, J. (2003). Thermally driven circulations in small oceanic basins. *Journal of Physical Oceanography*, *33*(11), 2333–2340. https://doi.org/10.1175/1520-0485(2003)033<2333:tdciso>2.0.co;2

Pickart, R. S., & Spall, M. A. (2007). Impact of Labrador Sea convection on the North Atlantic meridional overturning circulation. *Journal of Physical Oceanography*, *37*(9), 2207–2227. https://doi.org/10.1175/JPO3178.1

Sayol, J. M., Dijkstra, H., & Katsman, C. (2019). Seasonal and regional variations of sinking in the subpolar North Atlantic from a high-resolution ocean model. *Ocean Science*, *15*(4), 1033–1053. https://doi.org/10.5194/os-15-1033-2019

Send, U., & Marshall, J. (1995). Integral effects of deep convection. *Journal of Physical Oceanography*, *25*, 855–872. https://doi.org/10.1175/1520-0485(1995)025<0855:ieodc>2.0.co;2

Spall, M. A. (2003). On the thermohaline circulation in at bottom marginal seas. *Number 1 Journal of Marine Research*, *61*. https://doi.org/10.1357/002224003321586390

Spall, M. A. (2004). Boundary currents and watermass transformation in marginal seas. *Journal of Physical Oceanography*, *34*(5), 1197–1213. https://doi.org/10.1175/1520-0485(2004)034<1197:bcawti>2.0.co;2

Spall, M. A. (2008). Buoyancy-forced downwelling in boundary currents. *Journal of Physical Oceanography*, *38*(12), 2704–2721. https://doi.org/10.1175/2008JPO3993.1

Spall, M. A. (2010). Dynamics of down welling in an eddy-resolving convective basin. *Journal of Physical Oceanography*, *40*(10), 2341–2347. https://doi.org/10.1175/2010JPO4465.1

Spall, M. A., & Pickart, R. S. (2001). Where does dense water sink? A subpolar gyre example. *Journal of Physical Oceanography*, *31*(3), 810–826. https://doi.org/10.1175/1520-0485(2001)031<0810:wddwsa>2.0.co;2

Straneo, F. (2006). On the connection between dense Water formation, overturning, and Poleward heat transport in a convective basin. *Journal of Physical Oceanography*, *36*, 1822–1840. https://doi.org/10.1175/JPO2932.1

Suginohara, N. (1982). Coastal upwelling: Onshore–offshore circulation, Equatorward coastal jet and Poleward undercurrent over a continental shelf-slope. *Journal of Physical Oceanography*, *12*, 272–284. https://doi.org/10.1175/1520-0485(1982)012<0272:cuocec>2.0.co;2

Szekely, T., Gourrion, J., Pouliquen, S., & Reverdin, G. (2019). CORA, Coriolis ocean dataset for reanalysis. *SEANOE*. https://doi.org/10.17882/46219

Tagklis, F., Bracco, A., Ito, T., & Castelao, R. M. (2020). Submesoscale modulation of deep water formation in the Labrador Sea. *Scientific Reports*, *10*(1), 1–13. https://doi.org/10.1038/s41598-020-74345-w

Våge, K., Pickart, R. S., Sarafanov, A., Knutsen, Ø., Mercier, H., Lherminier, P., et al. (2011). The Irminger Gyre: Circulation, convection, and interannual variability. *Deep-Sea Research Part I Oceanographic Research Papers*, *58*(5), 590–614. https://doi.org/10.1016/j.dsr.2011.03.001